scientific reports

OPEN

Multifractal investigation of Ag/DLC nanocomposite thin films

Ştefan Ţălu [1], Bandar Astinchap[2,3], Senour Abdolghaderi [4,5✉], Azizollah Shafiekhani [4] & Ilya A. Morozov [6]

The objective of this study is the experimental investigation of the silver in diamond-like carbon (Ag/DLC) nanocomposite prepared by the co-deposition of radio frequency plasma-enhanced chemical vapor deposition (RF-PECVD) and RF-sputtering. Atomic force microscopy (AFM), X-ray diffraction analyses, ultraviolet–visible (UV–visible) spectroscopy measurements were applied to describe the three-dimensional surface texture data in connection with the statistical, and multifractal analyses. Additional information about structure–property relationships in prepared Ag/DLC nanocomposite was studied in detail to allow a better understanding of the surface micromorphology. The performed analysis revealed the studied samples have multifractal properties and can be included in novel algorithms for graphical representation of complex geometrical shapes and implemented in computer simulation algorithms.

Abbreviations

Ag/DLC	Silver in diamond like carbon
RF-PECVD	Radiofrequency plasma-enhanced chemical vapor deposition
AFM	Atomic force microscopy
XRD	X-ray diffraction
UV–visible	Ultraviolet–visible
LSPR	Localized surface plasmon resonance
3D	Three dimensional
NPs	Nanoparticles
FTIR	Fourier transform infrared
RMS	Root mean square
ACF	The autocorrelation function
HHCF	The height–height correlation function
PSDF	The power spectral density function

In the last decades, considerable progress has been made in the development of theoretical and computational methods to characterize the silver in diamond-like carbon (Ag/DLC) nanocomposite microstructures at the nanoscale in both the academic world and industry, because these films offer a wide range of exceptional physical, mechanical, and tribological properties.

Manninen et al.[1] studied the Ag–DLC coatings deposited by magnetron sputtering to evaluate: the Ag nanoparticle size distribution along the coatings thickness and the silver stability in DLC coatings.

Goto[2] reported results concerning the characteristics and tribological properties of both Ag/DLC nanocomposite coatings and Cu/DLC nanocomposite coatings with hydrogen-free DLC matrix deposited by RF magnetron sputtering using a concentric composite target.

Wu et al.[3] studied the doping effects of Ag concentration on microstructure, mechanical and vacuum tribological properties of the DLC films.

Ji et al.[4] investigated trace Ag–Ti co-doped DLC films prepared on stainless steel and silicon (100) substrates by medium frequency unbalanced magnetron sputtering and described the effects of sputtering current of Ti target on the microstructure, mechanical and tribological properties.

[1]The Directorate of Research, Development and Innovation Management (DMCDI), Technical University of Cluj-Napoca, 15 Constantin Daicoviciu St., 400020 Cluj-Napoca, Cluj County, Romania. [2]Department of Physics, University of Kurdistan, 66177-15175 Sanandaj, Iran. [3]Research Center for Nanotechnology, University of Kurdistan, 66177-15175 Sanandaj, Iran. [4]Department of Physics, Alzahra University, Vanak, 1953833511 Tehran, Iran. [5]Department of Education, Kurdistan Province, Sanandaj, Iran. [6]Institute of Continuous Media Mechanics UB RAS, 1 Korolev St., 614013 Perm, Russia. ✉email: s.abdolghaderi@gmail.com

Venkatesh et al.[5] prepared Ag-doped hydrogenated carbon thin films by a hybrid PVD–PECVD deposition process and observed that the working pressure and CH_4/Ar ratio played a key role in controlling the Ag content in DLC.

Abdolghaderi et al.[6] deposited Ag-DLC on glass and silicon substrates by the co-deposition of RF-sputtering and RF-sputtering method and studied electrical percolation threshold in nanocomposites.

Stach et al.[7] applied a stereometric analysis of 3D surfaces of the Ag–DLC nanocomposite films fabricated by Radio FrequencyPlasma-Enhanced Chemical Vapour Deposition (RF-PECVD).

Ţălu et al.[8] investigated the effects of deposition time on the nanoscale patterns of Ag/DLC nanocomposite synthesized by RF-PECVD and found the fractal dimension decreases with the increase of the deposition times on samples.

Ţălu et al.[9] studied the topographic uniformity, the fractal parameters of succolarity, the lacunarity coefficient, and the Shannon entropy of Ag/DLC composite synthesized by RF-PECVD for a better understanding of the structure–property correlation.

Baba et al.[10] prepared Ag-containing DLC films by a process combining reactive magnetron sputtering with plasma source ion implantation and observed that the structure and tribological properties were affected by the Ag content of the DLC films.

Jastrzębski et al.[11] reviewed previously published experimental data concerning mechanical and physicochemical properties of DLC coatings doped with Ag, Si, Cu, Ti, Ca, F and P as candidates for biomedical applications.

Cloutier et al.[12] studied Ag–DLC prepared in a hybrid plasma reactor and proposed a mechanism for Ag–DLC growth by plasma.

Wen et al.[13] reviewed many synthesis methods of DLC films, research theories and analysis methods applied in biomedical field.

A correct knowledge of the surface microtexture of thin films is a key factor to predict the suitability of the material for the proposed application[14–17]. The surface morphology describing the irregular surface geometry in terms of its space-filling ability can be estimated by fractal/multifractal analyses with a minimal set of fractal/multifractal parameters[18–22].

Information on the micro/nano scale surface microtexture has important implications for optimal design and offers new possibilities for investigating precise topographic and spatial characteristics[23–26]. Atomic force microscopy (AFM) is a useful tool for sampling real surface heights to determine complex spatial characteristics of a given surface[27–30]. AFM combined with image processing techniques can be used to further extract particular patterns in three dimensional (3D) complexities[31–33].

The present investigation attempts to explore insights into the multifractal nature of the Ag/DLC nanocomposite prepared by the co-deposition method of RF-PECVD and RF-sputtering using AFM analysis in connection with their surface morphology.

Methods

Materials and synthesis. The Ag–DLC nanocomposite films were fabricated by the co-deposition of RF-PECVD and RF-sputtering in a chamber.

The chamber consists of two electrodes with different area, a silver disc (4 cm diameter) was the smaller electrode as a powered electrode and the other electrode disc (a 13 cm diameter) holding the substrates was grounded via the body of the stainless-steel chamber. The distance between electrodes was 5 cm. A capacitance coupled RF system with a 13.56 MHz and 160 W power supply and bias voltage 80 V. Acetylene gas was used as reactive and bombarding gas in the RF plasma system. Deposition was done on glass and silicon substrates on the grounded electrode at room temperature. The chamber was evacuated to a base pressure of about 10^{-3} Pa before the deposition and then the pressure rises to 4 Pa pressure using only acetylene gas.

The three samples #1, #2, and #3 were deposited on 1 cm × 1 cm glass and silicon substrates at different deposition times of 10, 25, and 40 min respectively. Chamber pressure changes in the sputtering process for samples are shown in Fig. 1.

As can be seen in the deposition diagram (Fig. 1) all three samples follow the same pressure reduction pattern. So that, at first pressure is decreased, which is due to the deposition of hydrocarbons from acetylene plasma, after that the pressure is increased and it's because of the presence of the silver atom in the chamber and its deposition in films.

Prepared samples were characterized by X-ray diffraction (XRD) (Philips analytical with CoKα X-ray source (λ = 0.154 nm)), UV–VISIBLE (Stellar-Net EPP2000 UVN-SR), and AFM with instrument model DMC DS 95 series in non-contact mode.

The multifractal analysis was applied to AFM images for the characterization of surface morphology.

Results and discussion

UV–visible spectroscopy measurements. UV–visible spectroscopy of samples in 350–850 nm range is shown in Fig. 2. It is observed that in the absorption spectrum for all three samples the peak appears. This peak is related to localized surface plasmon resonance (LSPR) of Ag nanoparticles, which confirms the presence of Ag nanoparticles in prepared samples.

The absorption spectrum shows the position of the LSPR peaks has changed with increasing deposition time. This redshift of plasmon peak represents an increase in particle size with deposition time. Scaling up and aggregation of silver nanoparticles (NPs) on the surface of thin films (sample #1 to #3) cause to symmetry broking of spherical silver NPs then quadrupole and multipole show up in the absorbance spectrum.
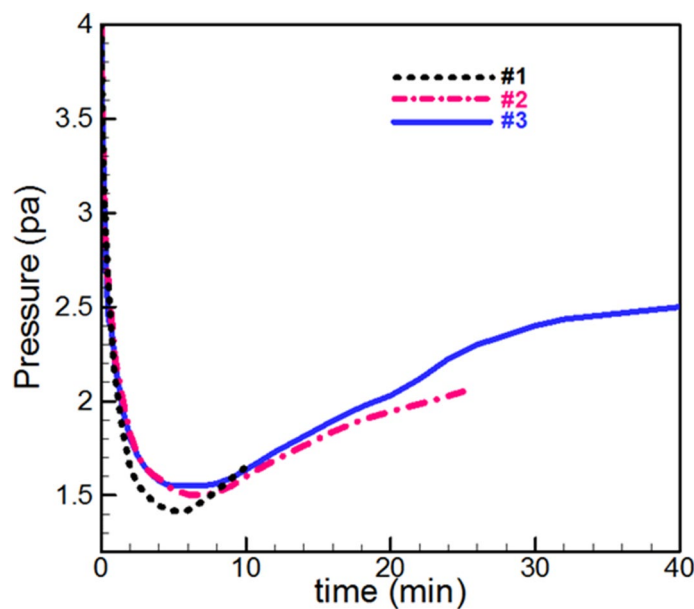
Figure 1. Deposition pressure diagram of the chamber (Pa) versus time of deposition (min) for samples #1 to #3.
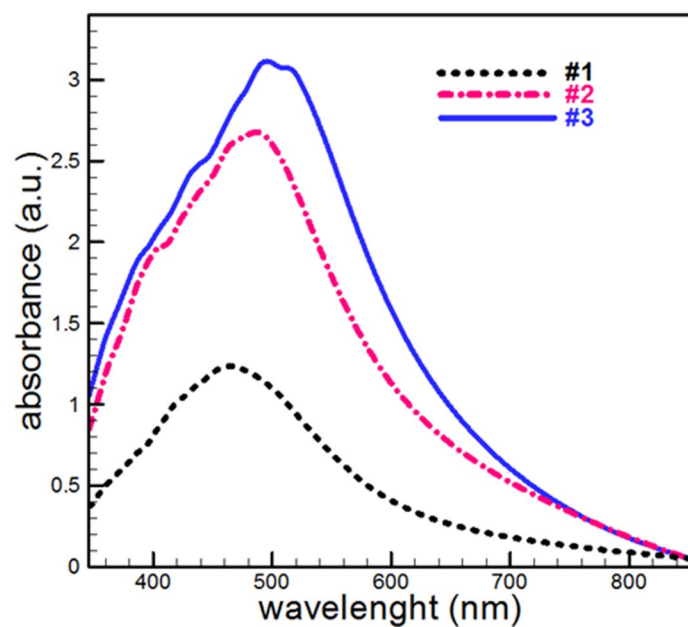
Figure 2. Absorption spectrum of fabricated samples.

Sample	Deposition time (min)	Plasmon position Wavelength (nm)	Sp^2/sp^3	Resistance ($\times 10^{-12}$ Ω cm)	Size of NPs (nm)
#1	10	458.46	0.69	5.94	7
#2	25	517.30	0.15	5.52	15
#3	40	519.74	0.089	1.97	22

Table 1. Obtained parameters from characterization of samples.
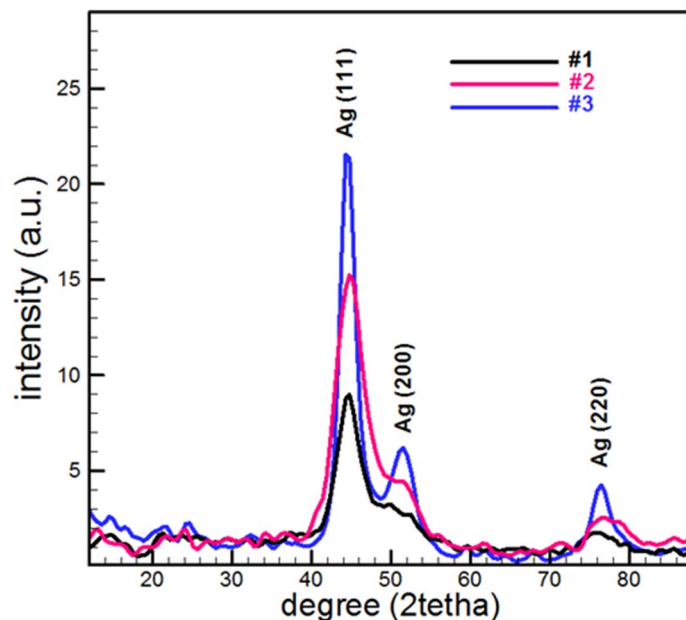
Figure 3. Typical XRD patterns of prepared Ag–DLC nanocomposites.

The Sp²/Sp³ ratio obtained from Fourier transform infrared (FTIR) spectroscopy is listed in Table 1. The peak in 2800–3100 cm⁻¹ range is attributed to C–H, and C–C bonding, and the area of normalized Gaussian's peak related to the C–H, and C–C bonding amount.

The obtained result shows that the sp²/sp³ ratio decrease with an increase in deposition time, which means the sp³ bond decreases, and the pseudo-diamond behavior of the samples is reduced. The sp² bond is directly proportional to the number of silver nanoparticles in the nanocomposites. Based on this, sample #3 has silver NPs more rather than #2 and #2 more than #1[14].

These results emphasize the previous discussion in UV–Vis analysis and deposition pressure diagram that the size (or amount) of the silver NPs increases with increasing deposition time.

XRD analysis.   To determine the crystalline structure of the specimens STOE-XRD diffractometer using Cu-Kα line ($\lambda = 0.154$ nm) was used.

The XRD patterns of prepared samples are shown in Fig. 3. The crystals planes with related Miller indices correspond to peaks are determined in XRD patterns. Based on reference cards, all peaks that appeared in the XRD patterns are consistent with the peaks of silver nanoparticles with a Face-centered cubic structure. The increase of particle size with deposition time from Sherrer relation is obvious (Table 1).

Obtained results from XRD analysis are in good agreement with other analyses to confirm the presence of silver nanoparticles in thin films and increasing the size of that with deposition time.

AFM measurements.   The samples were measured by Veeco di CP-II Atomic Force Microscope in contact mode. CONT20A-CP tips were used for scan areas set on 0.5 μm × 0.5 μm size, with 1 Hz scan rate and 256 × 256 pixel resolution.

For data analysis, the WSxM ver 5.0 software was used. Representative AFM images of rough substrates and their surface topography are shown in Fig. 4. The AFM pictures show whenever the deposition time is less the Ag nanoparticles are small in size and distributed almost uniformly and we have an almost regular network of particles embedded in DLC (Fig. 4a). Increasing the time of deposition, Ag nanoparticles distributed more and each site of particles became closer. In this stage of deposition close particles are associated or aggregated and form bigger particles with a large distance between newly formed ones. As one can see in Fig. 4b there is a small and big size of particles next to each other. In the next stage, the new small particles deposit and occupy a place in the distance between bigger particles (Fig. 4c). Particle size and location distribution changed relative with the time duration of deposition. Dependence of root mean square (RMS) roughness v.s. size of the observation window was calculated (Fig. 5).

Multifractal analysis of AFM images.   To characterize a multifractal system, we assume that the surface contains $N(\varepsilon)$ quadrate cells, with side ε and $r_i(\varepsilon) = \Sigma z_{kl}$ is the cumulative fluctuation of height around the mean value in the i-th square. A statistical sum can be defined as[21–23]:
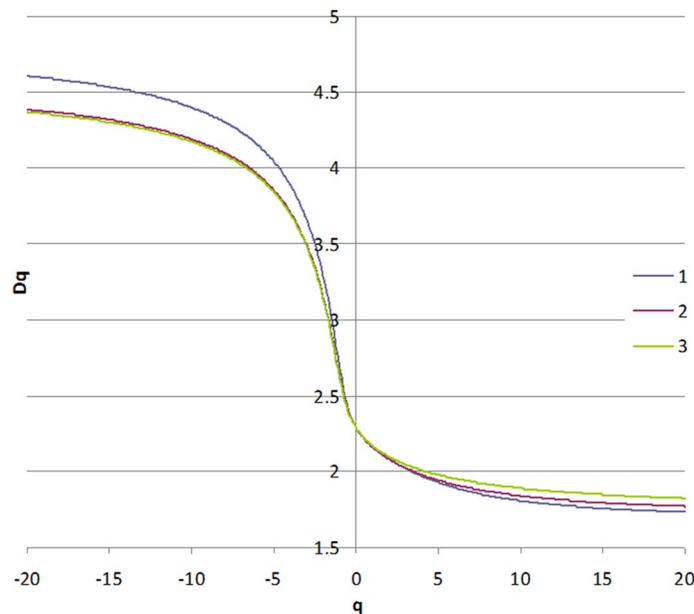
$$Z(q, \varepsilon) = \sum_{i=1}^{N(\varepsilon)} p_i^q(\varepsilon) \sim \varepsilon^{\tau(q)}, \tag{1}$$
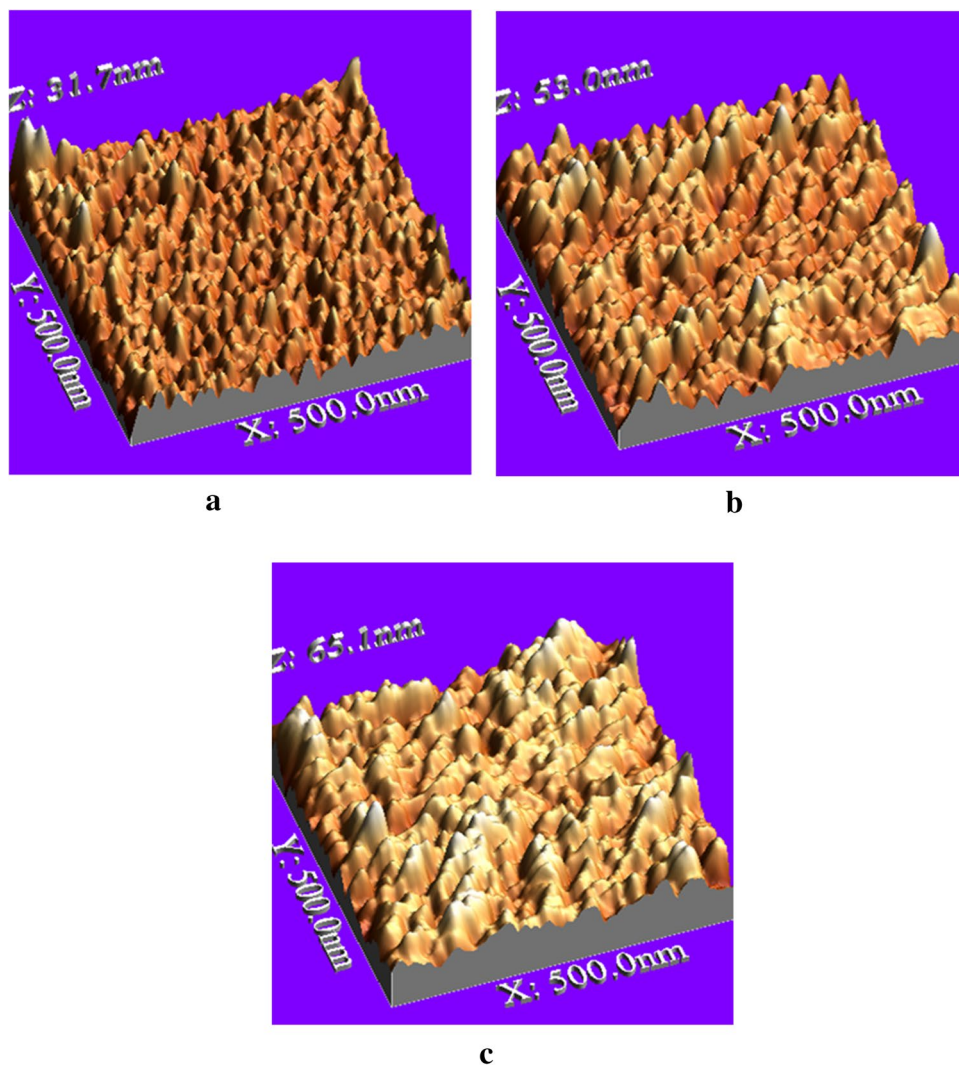
Figure 4. Representative AFM images of samples: (**a**) #1, (**b**) #2 and (**c**) #3 (WSxM ver 5.0 software, http://www.wsxm.es/).
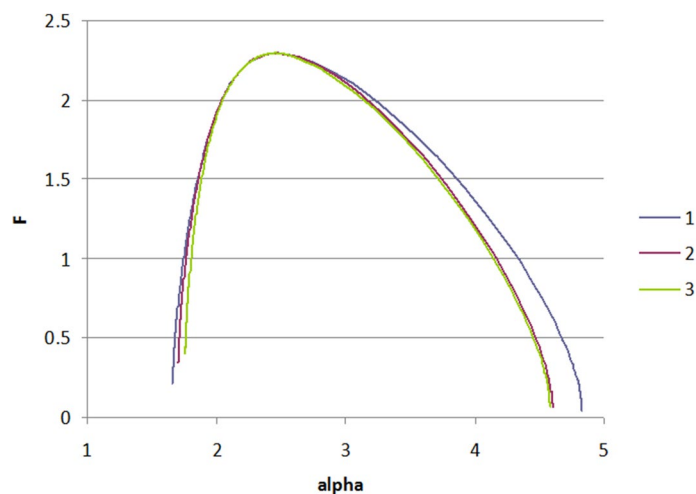
Figure 5. The graphical representation of RMS roughness of samples #1, #2 and #3 deposited at various times 10, 25 and 40 min.

Figure 6. The graphical representation of the multifractal singularity spectra f(α) of samples #1, #2 and #3 deposited at various times 10, 25 and 40 min.

where $p_i(\varepsilon) = r_i(\varepsilon)/\sum_{k=1}^{N(\varepsilon)} r_k(\varepsilon)$ and the power exponent $q \in (-\infty; +\infty)$.

The generalized fractal dimensions can be expressed in function of the mass exponent $\tau(q)$ as:

$$D_q = \tau(q)/(q-1). \tag{2}$$

The mass exponent $\tau(q)$ can be defined as:

$$\tau(q) = q\alpha(q) - f(\alpha(q)) \tag{3}$$

Equation (2) is usually written in terms of D_q as:

$$\alpha(q) = d\tau(q)/dq. \tag{4}$$

Multifractal singularity spectra $f(\alpha)$ shows the contribution of each monofractal in the whole structure for samples #1, #2, and #3 and represented by characteristic curves with a specific concave shape (non-linear and asymmetric form), and with different width spectrum $\Delta\alpha$, (and invariably with two arms); these are graphically represented in Fig. 6. The left shoulder of the multifractal singularity spectrum $f(\alpha)$ is much shorter than the right one. It can be noted that the variability of shapes of the morphological objects can be estimated by the maximal height of the $f(\alpha)$ spectrum (given by the D_0 value) and the multifractal width spectrum $\Delta\alpha = \alpha_{max} - \alpha_{min}$. α_q represents Hölder exponents of the qth order moment. In addition, for all samples, $\Delta\alpha > 0$. Analyzing $f(\alpha)$ curves, we can note that sample #2 and sample 3# are very close, i.e. multifractal spectrum not changed. Sample #1 has a higher contribution of small-sized monofractals, i.e. small relief features with the given fractal properties.

Generalized fractal dimensions D_q are shown in Fig. 7, with specific shapes of the D_q curves that are corresponding to typical multifractal surface morphology. The generalized fractal dimensions D_q was computed in the range $-20 \le q \le 20$. On the other hand, the right shoulder of the multifractal singularity spectrum $f(\alpha)$ for the #1 sample is much longer than of all the other samples, respectively. Also, the left arm of the multifractal spectrum corresponds to strongly irregular areas, defined by a high dimension value, while the right arm of $f(\alpha)$ is associated with flat zones. These shapes revealed that the surface morphology substantially changed. It can be seen that for all the samples, the capacity (or box-counting) dimension $D_0 = 2.29$.

The transition from a deposition time 1 to 2 (and 3) affected small peculiarities of relief: D_q for #1 lies higher at $q < 0$ than for #2 and #3.

For samples #2 and #3 the deposition time does not affect small-scale features: at q < 0 these graphs D_q are close; some deviations observed at $q > 0$, i.e. treatment slightly affected only large features of the surface.

Analyzing $f(\alpha)$ curves, we can note that #2 and 3# are very close, i.e. multifractal spectrum not changed. #1 has a higher contribution of small-sized monofractals.

The highest non-uniformity is observed for the sample with a deposition time of 10 min (#1) and lowest for the sample with a deposition time of 40 min (#3).

All this means that multifractals nucleate at a small deposition time, further treatment increases the size of objects without changing the multiscale properties.
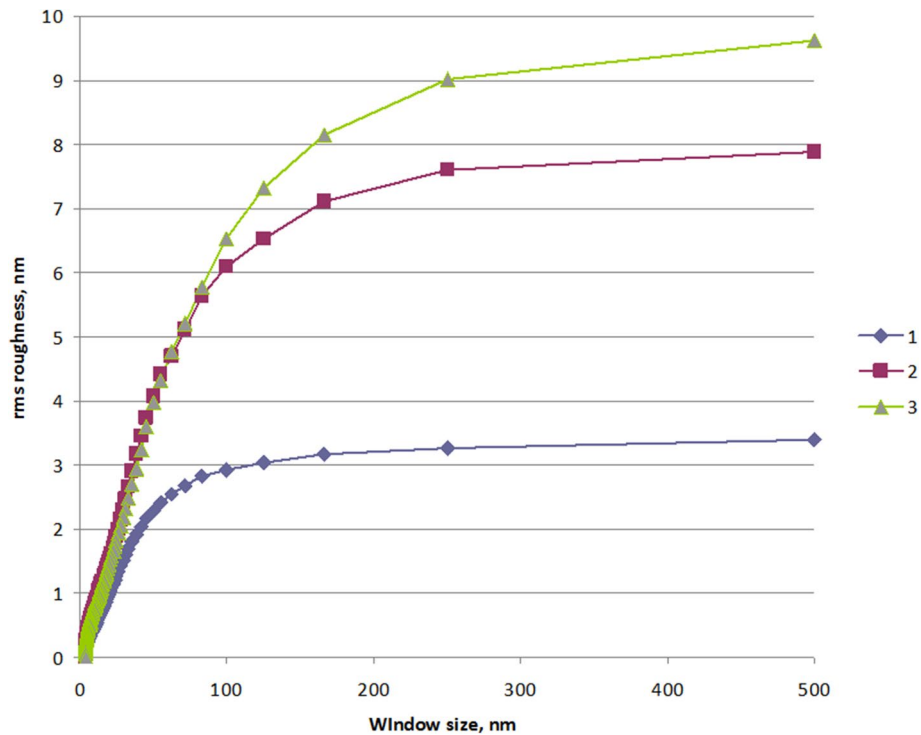
Figure 7. The graphical representation of the generalized fractal dimension Dq of samples #1, #2 and #3 deposited at various times 10, 25 and 40 min.

Statistical functions applied in the analysis of AFM images. A surface can be described by a height function, $h(r) \equiv h(x,y)$ where the height is measured from a fixed reference frame, and $r = (x,y)$ is any point on the surface.

The connection or correlation of spatially separated surface points can be computed by the autocorrelation (ACF) or height–height correlation (HHCF) function. The correlation length expresses the distance up to which the height of two surface points can be considered to be correlated.

The auto-correlation function, $R(r)$, is defined as[14,34]:

$$R(r) = \frac{1}{w^2} \frac{1}{L^2} \int_{-L/2}^{L/2} \int_{-L/2}^{L/2} \left[\{h(x,y) - \overline{h}\} \{h(x+x', y+y') - \overline{h}\} \right] dxdy \tag{5}$$

where r is the spatial separation between two arbitrary surface points, $r_1 = (x,y)$ and $r_2 = (x+\acute{x}, y+\acute{y})$.

For a truly random rough surface, $R(r)$ decays to zero with increasing r. The decay rate depends on the randomness of the surface.

The lateral correlation length, ξ, is defined as a length scale over which the magnitude of $R(r)$ decreases to $1/e$ of its value at $r = 0$, i.e., $R(\xi) = (1/e) R(0)$ spatial length over the surface at which this autocorrelation function drops down to $1/e$. If the distance r between two surface points is within lateral correlation length $r < \xi$, the heights at these two points can be considered to be correlated. If the distance r between two points is greater than ξ the height at these two points is considered to be independent of each other.

The height–height correlation function, $G(r)$, is defined as[14,34]:

$$G(r) = \frac{1}{L^2} \int_{-L/2}^{L/2} \int_{-L/2}^{L/2} \left[h(x+x', y+y') - h(x,y) \right]^2 dxdy \tag{6}$$

For a random rough surface, the height–height correlation function has the form[14,34]:
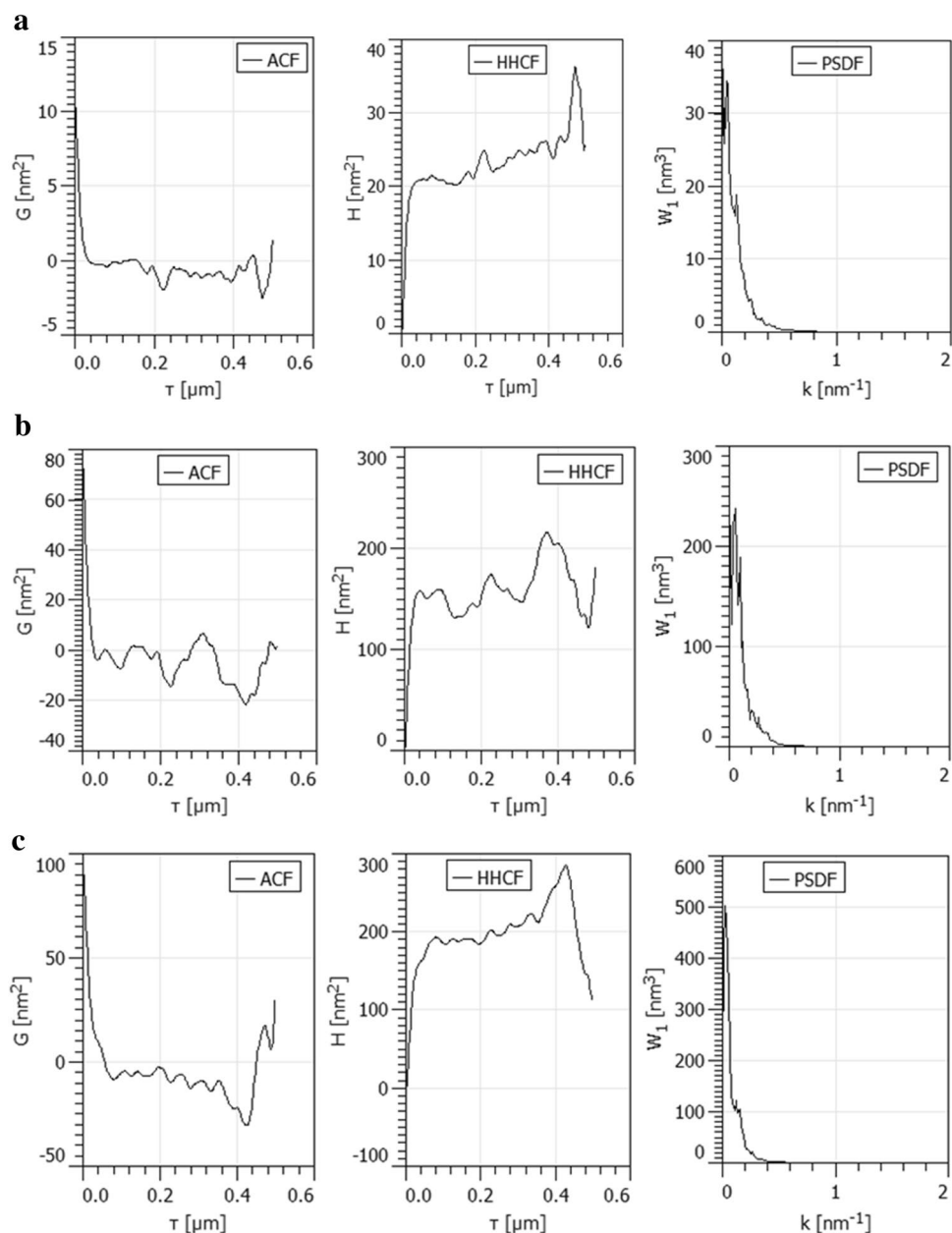
$$G(r) \approx r^{2\alpha} \, for \, r << \xi \tag{7}$$

$$G(r) \approx 2w^2 \, for \, r >> \xi \tag{8}$$

$R(r)$ and $G(r)$ are related by[14,34]:

$$G(r) \approx 2w^2 [1 - R(r)] \tag{9}$$

where α is the roughness exponent.

Figure 8. The ACF, HHCF and PSDF functions computed for samples (**a**) #1, (**b**) #2 and (**c**) #3 deposited at various times 10, 25 and 40 min (Gwyddion software, ver. 2.53, http://www.cmi.cz/).

The power spectrum or structure factor of the surface, $S(k)$, is the square of the Fourier transform of the surface height profile $h(x,y)$ and can be expressed as[14,34]:

$$S(k) = \frac{1}{L^2} \left| \int_{-L/2}^{L/2} \int_{-L/2}^{L/2} \left[\{ h(x+x', y+y') - h(x,y) \} e^{-i(k_x x + k_y y)} \right] dx dy \right|^2 \tag{10}$$

If the surface height fluctuation is periodic with a repetition length, l, the periodicity will be reflected in the power spectrum $S(k)$ as a peak at the wavenumber $k = 2\pi/l$.

To understand the nature of the surface micro-textures in detail, extensive analysis of AFM images was carried out using the Gwyddion software ver. 2.53[34]. The second-order statistical quantities observing the mutual relationship of two points on the surface are employed in analyses[34].

The statistical functions (the autocorrelation function—ACF, the height–height correlation function—HHCF, the power spectral density function—PSDF) computed for samples are shown in Fig. 8.

It can be seen that the ACF and HHCF functions of all samples are characterized by the high speed of data variation. The PSDF functions for all samples have similar graphical variations. The graphical statistical functions

confirm the multifractal results and these are highly correlated at this scale. In these areas, surface microtexture is heterogeneous, containing sub-regions of different micropatterns.

Conclusions

The surface microtexture characteristics of Ag/DLC nanocomposite prepared by RF-PECVD and RF-sputtering co-deposition method was quantitatively investigated using AFM together with the 3-D surface micromorphology and multifractal analyzes. The study revealed a nanometer multifractal nature of the samples.

Statistical and multifractal analysis of the surface height function observed by the AFM experiments provides information about the development of surface morphology with the sample deposition times. Generalized fractal dimension, multifractal singularity spectra, and statistical functions show results consistent with the XRD and UV–visible spectroscopy measurements. From experimental topography data, and appropriate analyses, the effectiveness, and accuracy of our approach have been demonstrated.

AFM observation of the surfaces showed the growth of nanosized features as the deposition time increases. The multifractal analysis revealed that these objects have fractal nature which is unchanged as the deposition time rises: small fractals appear at the initial stage of plasma treatment and then become larger without altering the fractal properties. On the basis of these findings, the results presented here could have a great impact on the development of advanced materials with new potential applications in fields as diverse as sensors, tribology, and biomaterials can be found.

Data availability

The datasets analyzed during the current study are available from the corresponding author on reasonable request.

References

1. Manninen, N. K., Galindo, R. E., Carvalho, S. & Cavaleiro, A. Silver surface segregation in Ag-DLC nanocomposite coatings. *Surf. Coat. Technol.* **267**, 90–97. https://doi.org/10.1016/j.surfcoat.2014.12.029 (2015).
2. Goto, M. Preparations and tribological properties of soft-metal/DLC composite coatings by RF magnetron sputter using composite targets. *Int. J. Mech. Mater. Des.* **14**, 313–327. https://doi.org/10.1007/s10999-017-9376-3 (2018).
3. Wu, Y. *et al.* Preparation and properties of Ag/DLC nanocomposite films fabricated by unbalanced magnetron sputtering. *Appl. Surf. Sci.* **284**, 165–170. https://doi.org/10.1016/j.apsusc.2013.07.074 (2013).
4. Ji, L. *et al.* The role of trace Ti concentration on the evolution of microstructure and properties of duplex doped Ti(Ag)/DLC films. *Vacuum* **115**, 23–30. https://doi.org/10.1016/j.vacuum.2015.01.023 (2015).
5. Venkatesh, M., Taktak, S. & Meletis, E. I. Synthesis of Ag-doped hydrogenated carbon thin films by a hybrid PVD–PECVD deposition process. *Bull. Mater. Sci.* **37**(7), 1669–1676 (2014).
6. Abdolghaderi, S., Astinchap, B. & Shafiekhani, A. Electrical percolation threshold in Ag–DLC nanocomposite films prepared by RF-sputtering and RF-PECVD in acetylene plasma. *J. Mater. Sci. Mater. Electron.* **27**, 6713–6720. https://doi.org/10.1007/s10854-016-4620-4 (2016).
7. Stach, S., Ţălu, Ş, Abdolghaderi, S., Shafiekhani, A. & Bahmani, J. 3_D surface stereometry of Ag/DLC nanocomposite prepared by RF-PECVD. *Results Phys.* **15**, 1–8. https://doi.org/10.1016/j.rinp.2019.102731 (2019).
8. Ţălu, Ş, Stach, S. & Abdolghaderi, S. The effects of deposition time on the nanoscale patterns of Ag/DLC nanocomposite synthesized by RF-PECVD. *Microsc. Res. Tech.* **82**(5), 572–579. https://doi.org/10.1002/jemt.23203 (2019).
9. Ţălu, Ş, Abdolghaderi, S., Pinto, E. P., Matos, R. S. & Salerno, M. Advanced fractal analysis of nanoscale topography of Ag/DLC composite synthesized by RF-PECVD. *Surf. Eng.* **36**(7), 713–719. https://doi.org/10.1080/02670844.2019.1710937 (2020).
10. Baba, K., Hatada, R., Flege, S. & Ensinger, W. Preparation and properties of Ag-containing diamond-like carbon films by magnetron plasma source ion implantation. *Adv. Mater. Sci. Eng.* https://doi.org/10.1155/2012/536853 (2012).
11. Jastrzębski, K., Jastrzębska, A. & Bociąga, D. A review of mechanical properties of diamond-like carbon coatings with various dopants as candidates for biomedical applications. *Acta Innov.* **22**, 40–57 (2017).
12. Cloutier, M. *et al.* Controlled distribution and clustering of silver in Ag–DLC nanocomposite coatings using a hybrid plasma approach. *ACS Appl. Mater. Interfaces* **8**(32), 21020–21027. https://doi.org/10.1021/acsami.6b06614 (2016).
13. Wen, F., Liu, J. & Xue, J. The studies of diamond-like carbon films as biomaterials. *Rev. Colloid Surf. Sci.* **2**(3), 81–95. https://doi.org/10.11648/j.css.20170203.11 (2017).
14. Ţălu, Ş. *Micro and Nanoscale Characterization of Three Dimensional Surfaces. Basics and Applications* (Napoca Star Publishing House, Cluj-Napoca, 2015).
15. Ramazanov, S., Ţălu, Ş, Sobola, D., Stach, S. & Ramazanov, G. Epitaxy of silicon carbide on silicon: Micromorphological analysis of growth surface evolution. *Superlatt. Microstruct.* **86**, 395–402. https://doi.org/10.1016/j.spmi.2015.08.007 (2015).
16. Elenkova, D. *et al.* Morphology and optical properties of SiO₂-based composite thin films with immobilized terbium(III) complex with a biscoumarin derivative. *Int. J. Polym. Anal. Charact.* **20**, 42–56. https://doi.org/10.1080/1023666X.2014.955042 (2015).
17. Arman, A. *et al.* Micromorphology characterization of copper thin films by AFM and fractal analysis. *J. Mater. Sci. Mater. Electron.* **26**, 9630–9639. https://doi.org/10.1007/s10854-015-3628-5 (2015).
18. Stach, S. *et al.* Morphological features in aluminum nitride epilayers prepared by magnetron sputtering. *Mater. Sci. Pol.* **33**, 175–184. https://doi.org/10.1515/msp-2015-0036 (2015).
19. Ţălu, Ş *et al.* Multifractal spectra of atomic force microscope images of Cu/Fe nanoparticles based films thickness. *J. Electroanal. Chem.* **749**, 31–41. https://doi.org/10.1016/j.jelechem.2015.04.009 (2015).
20. Yadav, R. P., Dwivedi, S., Mittal, A. K., Kumar, M. & Pandey, A. C. Fractal and multifractal analysis of LiF thin film surface. *Appl. Surf. Sci.* **261**, 547–553. https://doi.org/10.1016/j.apsusc.2012.08.053 (2012).
21. Ţălu, Ş *et al.* Topographic characterization of Cu–Ni NPs @ a-C: H films by AFM and multifractal analysis. *J. Phys. Chem. B.* **119**, 5662–5670. https://doi.org/10.1021/acs.jpcb.5b00042 (2015).
22. Ţălu, Ş *et al.* Multifractal characterization of water soluble copper phthalocyanine based films surfaces. *Electron Mater Lett.* https://doi.org/10.1007/s13391-013-3270-4 (2014).
23. Ţălu, Ş *et al.* Multifractal analysis of drop-casted copper (II) tetrasulfophthalocyanine film surfaces on the indium tin oxide substrates. *Surf. Interface Anal.* **46**(6), 393–398. https://doi.org/10.1002/sia.5492 (2014).

24. Solaymani, S. *et al.* Characterization of microroughness parameters in Cu-C nanocomposite prepared by co-deposition of RF-sputtering and RF-PECVD. *Eur. Phys. J. Appl. Phys.* **64**(01), 11301. https://doi.org/10.1051/epjap/2013130121 (2013).
25. Ţălu, Ş *et al.* Gold nanoparticles embedded in carbon film: micromorphology analysis. *J. Ind. Eng. Chem.* **35**, 158–166. https://doi.org/10.1016/j.jiec.2015.12.029 (2016).
26. Stach, S. *et al.* Stereometric parameters of the Cu/Fe NPs thin films. *J. Phys. Chem. C* **119**(31), 17887–17898. https://doi.org/10.1021/acs.jpcc.5b04676 (2015).
27. Zare, M. *et al.* Evolution of rough surface geometry and crystalline structures of aligned TiO$_2$ nanotubes for photoelectrochemical water splitting. *Sci. Rep.* **8**, 1–11. https://doi.org/10.1038/s41598-018-29247-3 (2018).
28. Dallaeva, D. *et al.* AFM imaging and fractal analysis of surface roughness of AlN epilayers on sapphire substrates. *Appl. Surf. Sci.* **312**, 81–86. https://doi.org/10.1016/j.apsusc.2014.05.086 (2014).
29. Ţălu, Ş *et al.* Microstructure and micromorphology of Cu/Co nanoparticles: Surface texture analysis. *Electron. Mater. Lett.* **12**(5), 580–588. https://doi.org/10.1007/s13391-016-6036-y (2016).
30. Sobola, D., Ţălu, Ş, Solaymani, S. & Grmela, L. Influence of scanning rate on quality of AFM image: Study of surface statistical metrics. *Microsc. Res. Tech.* https://doi.org/10.1002/jemt.22945 (2017).
31. Méndez, A., Reyes, Y., Trejo, G., Stępień, K. & Ţălu, Ş. Micromorphological characterization of zinc/silver particle composite coatings. *Microsc. Res. Tech.* **78**, 1082–1089. https://doi.org/10.1002/jemt.22588 (2015).
32. Stach, S. *et al.* 3D surface stereometry studies of sputtered TiN thin films obtained at different substrate temperatures. *J. Mater. Sci. Mater. Electron.* **28**(2), 2113–2122. https://doi.org/10.1007/s10854-016-5774-9 (2017).
33. Mwema, F. M. *et al.* Advances in manufacturing analysis: fractal theory in modern manufacturing. In *Modern Manufacturing Processes* vol 2 1st edn (eds Kumar, K. & Davim, J. P.) 13–39 (Woodhead Publishing Reviews: Mechanical Engineering Series, USA, 2020). https://doi.org/10.1016/B978-0-12-819496-6.00002-6.
34. Gwyddion software user guide, version 2.53, 2019. P. Klapetek, D. Necas, C. Anderson, Czech Metrology Institute, Brno, Czech Republic. http://www.cmi.cz/.

Author contributions

Ş.Ţ.: analysis and interpretation of data, and writing; B.A.: conception of the work and editing; A.S.: using software and substantively revised it; S.A.: experiments, acquisition and writing; I.A.M.: analysis and interpretation of data.

Competing interests

The authors declare no competing interests.

Additional information

Correspondence and requests for materials should be addressed to S.A.

Reprints and permissions information is available at www.nature.com/reprints.

Publisher's note Springer Nature remains neutral with regard to jurisdictional claims in published maps and institutional affiliations.